CHEMISTRY

Dissipative biocatalytic cascades and gated transient biocatalytic cascades driven by nucleic acid networks

Yu Ouyang, Pu Zhang, Itamar Willner*

Living systems consist of complex transient cellular networks guiding structural, catalytic, and switchable functions driven by auxiliary triggers, such as chemical or light energy inputs. We introduce two different transient, dissipative, biocatalytic cascades, the coupled glucose oxidase (GOx)/horseradish peroxidase (HRP) glucose–driven oxidation of 2,2′-azino-bis(3-ethylbenzothiazoline-6-sulfonic acid) ($ABTS^{2-}$) to the radical anion ($ABTS^{\bullet-}$) and the lactate dehydrogenase (LDH)/nicotinamide adenine dinucleotide (NAD^+) lactate–driven reduction of NAD^+ to NADH. The transient biocatalytic systems are driven by nucleic acid reaction modules using a nucleic acid fuel strand L_1' and a nicking enzyme, Nt.BbvCI, as fuel-degrading catalyst, leading to the dynamic spatiotemporal transient formation of structurally proximate biocatalysts activating the biocatalytic cascades and transient coupled processes, including the generation of chemiluminescence and the synthesis of alanine. Subjecting the mixture of biocatalysts to selective inhibitors allows the gated transient operation of the biocatalysts. The kinetics of transient biocatalytic cascades are accompanied by kinetic models and computational simulations.

INTRODUCTION

Living systems include complex transient, dissipative, cellular networks revealing structural, catalytic, and stimuli-responsive adaptive functions while consuming energy, such as chemical fuels or light (*1*–*3*). Processes including proliferation (*4*), cell motility (*5*), and operation of biocatalytic networks (*6*, *7*) represent such transient, out-of-equilibrium, chemical transformations. Within the general scope of systems chemistry, efforts are directed to emulate the principles of biological processes by synthetic chemical systems (*8*–*13*). For example, the carbodiimide-fueled dynamic assembly and dissipative depletion of anhydrides (*14*) or the catalytic formation and hydrolytic dissociation of peptides led to spatiotemporal formation of fibers (*15*). In addition, a pH-driven molecular rotaxane machine was used to stimulate, transient, dissipative catalysis (*16*), and feedback-driven programmed pH changes were used to control the sizes of polymersomes and create self-adaptive nanoreactors (*17*). Cyclic enzyme-catalyzed pH cycles were applied for the dynamic transient control of the shear properties of polymer fluids (*18*) or the stiffness of hydrogel materials (*19*, *20*). In addition, the guanosine triphosphate–driven growth and division of protein fibrils in coacervate droplets (*21*) or the light-responsive self-assembly of multicompartmentalized microsystems (*22*) demonstrated dynamic transient, dissipative, processes mimicking cell division.

The information encoded in the base sequence of nucleic acid dictates structural and functional properties of the biopolymer (*23*). The control over the stability of duplex nucleic acid by the nature and number of the base pairs guides the reconfiguration of double-stranded structure by the strand displacement mechanism (*24*), and sequence-specific recognition functions of nucleic acids (aptamers) (*25*) or sequence-dictated catalytic functions (DNAzymes) (*26*) were demonstrated. These functions of nucleic acids were applied to develop DNA switches (*27*), DNA machines (*28*, *29*), reconfigurable DNA nanostructures (*30*), and stimuli-responsive gated nanocarriers (*31*). In addition, DNA scaffolds were used for the programmed spatial organization of enzymes (*32*) and the activation of superior biocatalytic cascades on DNA scaffolds (*33*, *34*) and in confined nanoscale environments (*35*, *36*). In particular, nucleic acids provide a versatile material to assemble dynamic networks (*37*), revealing stimuli-responsive reconfiguration demonstrating adaptive (*38*, *39*), hierarchically adaptive (*40*), feedback (*41*), and intercommunicating functions (*42*). In addition, the recognition and catalytic properties of nucleic acid and their responsiveness to auxiliary enzymes, such as nicking enzymes or endonucleases, provide versatile means to design dynamic, transient, out-of-equilibrium systems (*43*–*45*). These included the fuel-driven transient DNA strand displacement circuitry with self-resetting functions (*46*), dissipative DNA-based aptamers for the transient loading and release of cargoes (*47*), the assembly of bistable genetic regulatory networks (*48*, *49*), the design of in vitro transcriptional oscillators (*50*, *51*), the design of transient nucleic acid structures controlled by redox inputs (*52*), and the assembly of dynamic DNAzyme-based circuitries (*53*). In addition, enzyme-guided activation of transient nucleic acid–based networks was demonstrated, including the nicking enzyme–activated dissipative gated and cascaded DNA network operations (*54*), the nicking enzyme–guided transient reconfiguration of constitutional dynamic networks (*55*), the nicking enzyme–activated transient control of the optical properties of Au nanoparticles and semiconductor quantum dots, through their dynamic dissipative aggregation and deaggregation by bridging nucleic acids (*56*), and the adenosine triphosphate–driven ligation of toehold-modified duplex nucleic acids and their dissipative separation by endonucleases (*57*).

In the present study, we use transient dissipative nucleic acid frameworks as functional modules to operate biocatalytic cascades and gated biocatalytic cascades. Previous studies have applied organized nucleic acid nanostructures, such as DNA strips (*58*), chains (*59*), or origami tiles (*60*), as scaffolds to organize biocatalysts and to guide the operation of biocatalytic cascades. In addition, nucleic acid machines such as tweezers (*61*) were used to switch biocatalytic cascades, and dynamically equilibrated constitutional dynamic networks were applied as functional modules to operate biocatalytic cascades (*62*). The transient nucleic acid–guided operation of biocatalytic cascades and particularly the gated transient activation of

The Institute of Chemistry, Center for Nanoscience and Nanotechnology, The Hebrew University of Jerusalem, Jerusalem 91904, Israel.
*Corresponding author. Email: itamar.willner@mail.huji.ac.il

biocatalytic cascades are, however, unprecedented. Such transient biocatalytic cascades could find important nanomedical applications by providing spatiotemporal activation of therapeutic enzymes. Note that in contrast to previous dynamic systems, where enzymes (or catalysts) guide the transient dissipative behavior of the networks, the present study introduces a means to apply the transient behavior of the nucleic acid networks to guide biocatalytic cascades or gated biocatalytic cascades by controlling the spatiotemporal proximity between the respective biocatalytic constituents.

RESULTS

Dynamically triggered transient glucose oxidase/horseradish peroxidase biocatalytic cascade

Figure 1 outlines the principle for operating the well-established glucose oxidase (GOx)/horseradish peroxidase (HRP) biocatalytic cascade. The reaction module I consists of a duplex nucleic acid L_1/T_1, the nucleic acid–modified biocatalysts consisting of GOx covalently linked to the nucleic acid A_1 (A_1-GOx) and HRP linked to the nucleic acid strand A_2 (A_2-HRP), and the nicking enzyme Nt.BbvCI. (For the synthesis of the single nucleic acid–modified biocatalysts and the evaluation of the purities of the DNA-enzyme hybrids, see figs. S1 to S3 and table S1.) The transient operation of the GOx/HRP cascade is activated by subjecting the reaction module I to the fuel strand L_1' that results in the displacement of the duplex L_1/T_1 to yield the duplex L_1'/L_1 and the strand T_1. The strands A_1 and A_2 are pre-engineered to include complementary domains to the strand T_1 to yield the supramolecular complex T_1/A_1-GOx+A_2-HRP. The proximity of the biocatalysts in the supramolecular complex results in the enhancement of the GOx/HRP biocatalytic cascade where GOx catalyzes the aerobic oxidation of glucose to produce gluconic acid and H_2O_2, and the H_2O_2 product is channeled into the HRP that catalyzes the oxidation of 2,2′-azino-bis(3-ethylbenzothiazoline-6-sulfonic acid) ($ABTS^{2-}$) to give the colored 2,2′-azino-bis(3-ethylbenzothiazoline-6-sulfonic acid) radical anion ($ABTS^{\bullet-}$) (Fig. 1, inset X). The duplex L_1'/L_1 is pre-engineered to include the sequence-specific nicking site for nicking enzyme, Nt.BbvCI. Cleavage of the strand L_1' leads to the separation of the fragmented products and the release of L_1. The released strand L_1 displaces T_1 from the supramolecular complex T_1/A_1-GOx+A_2-HRP, resulting in a process blocking the biocatalytic cascade and regenerating the original rest module. Thus, the fueled treatment of the reaction module leads to the transient and dissipative operation of the biocatalytic cascade. The transient operation of the system is a result of an appropriate dictated energetic balance of the constituents, guided by the relative stabilities of the structurally engineered constituents. That is, the mixture of duplexes consisting of L_1'/L_1 and T_1/A_1-GOx+A_2-HRP exhibits enhanced stability, as compared to the duplex L_1/T_1. The nicking of the duplex L_1'/L_1 yields two fragment strands that lack hybridization stability with L_1 and are separated as "waste" products. Upon displacement of T_1, the released L_1 forms the duplex L_1/T_1 that reveals a higher stability as compared to the supramolecular complex T_1/A_1-GOx+A_2-HRP, leading to the dynamic transient behaviors of the DNA framework and thus to the transient operation of the biocatalytic cascade. (For a further discussion on the relative energetics of the constituents in the system, see section S1.)

The transient operation of the biocatalytic cascade is followed spectroscopically by probing the transient absorbance features of $ABTS^{\bullet-}$ (λ = 420 nm) at time intervals of the transient operation of the scaffold (Fig. 2A, panels I and II). In this experiment, the aliquots of sample are taken out from the dynamic reaction mixture, and the temporal efficacy of the biocatalytic cascade associated with each aliquot is evaluated by following the time-dependent formation of $ABTS^{\bullet-}$. The transient absorbance changes of $ABTS^{\bullet-}$ (after a fixed time interval of 2 min) are presented in panel III. Using an appropriate calibration curve relating the absorbance of $ABTS^{\bullet-}$ generated by defined concentrations of the intermediate T_1/A_1-GOx+A_2-HRP (fig. S5), the time-dependent transient concentration changes of $ABTS^{\bullet-}$ at each time of the transient operation of the system are translated into temporal molar concentrations of the transient, dissipative, catalytic constituent T_1/A_1-GOx+A_2-HRP. The transient concentrations of T_1/A_1-GOx+A_2-HRP generated by the biocatalytic cascade driven by the fuel strand L_1', 6 μM, and nicking enzyme Nt.BbvCI, 0.046 μM, within the dynamic network were evaluated, and these are displayed in Fig. 2B [curve (i_a), solid point].

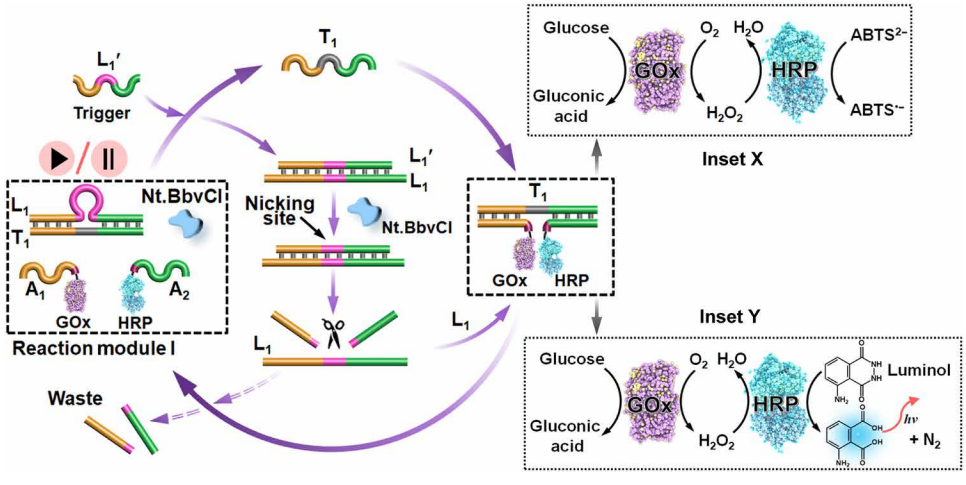

Fig. 1. Transient operation of the GOx/HRP biocatalytic cascade. Schematic operation of the transient GOx/HRP biocatalytic cascade driven by a nucleic acid–based machinery using reaction module I. Insets depict the conjugation of the transient GOx/HRP cascade to the GOx/HRP-driven transient generation of $ABTS^{\bullet-}$ (inset X) and chemiluminescence (inset Y).

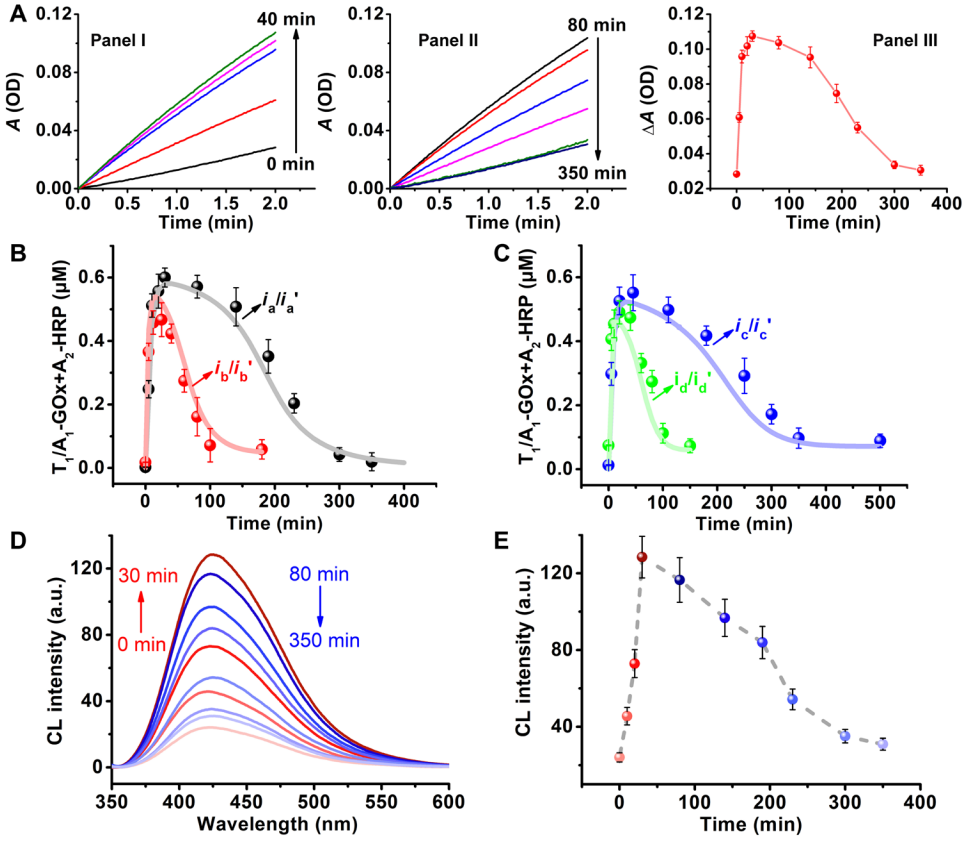

Fig. 2. Dynamic transient curves corresponding to the GOx/HRP cascade. (**A**) Time-dependent absorbance changes generated by the GOx/HRP cascade using glucose and the product, $ABTS^{\bullet-}$, as readout signal following the dissipative cycle shown in Fig. 1. Panel I and II: Transient processes from time $t = 0$ to 40 min and $t = 80$ to 350 min completing the transient biocatalytic cycle. Panel III: Transient absorbance changes corresponding to $ABTS^{\bullet-}$ after a fixed time interval of 2 min. Experimental conditions: T_1, L_1, A_1-GOx, and A_2-HRP = 1 μM; Nt.BbvCI = 0.046 μM; and $L_1' = 6$ μM. (**B**) Transient concentrations of constituent T_1/A_1-GOx+A_2-HRP, curve (i_a) (solid point) [concentrations derived by translating the results shown in (A) into transient absorbance changes of $ABTS^{\bullet-}$ and, subsequently, into transient concentrations of T_1/A_1-GOx+A_2-HRP using the calibration curve shown in fig. S5]. Solid curve (i_a'): Computationally simulated transient of curve (i_a) (solid point) using the kinetic model [fig. S6, curve (i_b')] represents the predicted dynamics of transient constituent T_1/A_1-GOx+A_2-HRP in the presence of trigger L_1' (3 μM) using the rate constants derived from (i_a). Curve (i_b): Experimental validation of the predicted results at the specified conditions. (**C**) Curves (i_c') and (i_d') predicted dynamic transient of T_1/A_1-GOx+A_2-HRP in the presence of Nt.BbvCI (0.0307 and 0.0765 μM), applying the rate constants derived from (i_a). Curves (i_c) and (i_d): Experimental validation of the predicted results (experimental conditions: T_1, L_1, A_1-GOx, and A_2-HRP = 1 μM and $L_1' = 6$ μM). (**D**) Time-dependent chemiluminescence (CL) spectra generated by the GOx/HRP transient biocatalytic reaction module shown in Fig. 1. a.u., arbitrary units. (**E**) Transient chemiluminescence intensities generated by the biocatalytic GOx/HRP cascade shown in Fig. 1 (inset Y). Chemiluminescence spectra were recorded in the presence of 5 mM glucose and 500 μM luminol. Error bars for all experiments derived from $N = 3$ experiments.

The transient dynamic behaviors of the biocatalytic cascade were computationally simulated using the kinetic model formulated in the figs. S6 and S7. The rate constants of the subreactions associated with the best-fit curve (i_a'), according to the kinetic model, are tabulated in table S2. The kinetic model and the resulting rate constants have a value if they can predict the dynamic behaviors of the system at different auxiliary conditions and provided that the predicted results are experimentally validated. As the dynamic process is anticipated to be controlled by the concentrations of the fuel strand L_1' and the nicking enzyme as auxiliary parameters, the transient biocatalytic cascades operating in the presence of L_1', 3 μM, (instead of 6 μM) and a fixed concentration of the nicking enzyme 0.046 μM was computationally simulated [Fig. 2B, curve (i_b'), solid curve] and experimentally validated [red point overlaid as curve (i_b), solid points]. For the effect of additional concentration ratios of the nucleic acid–modified enzymes/L_1' on the transient biocatalyst cascade, see fig. S8. Similarly, the transient biocatalytic cascade operating at a fixed concentration of L_1' equal to 6 μM was computationally simulated in the presence of the nicking enzyme at a concentration of 0.0307 μM [curve (i_c'), solid line; substituting the concentration of the nicking enzyme corresponding to 0.0765 μM, curve i_d/i_d'] and experimentally validated [red dots curve (i_c) overlaid on (i_c')]. Note that the time-dependent absorbance changes of $ABTS^{\bullet-}$ at the auxiliary parameters to drive the transient curves corresponding to curves (i_b-i_d) in Fig. 2 (B and C) are presented in fig. S9. Very good agreement between the experimental and predicted dynamic behaviors of the systems is demonstrated. We note that, upon increasing the concentration of the fuel strand L_1', the peak content of transient biocatalytic cascaded product increases and the dissipative time interval to the original module is slower. On the other hand, increasing the concentration of the nicking enzyme slightly decreases the peak content of the biocatalytic supramolecular complex, yet the transient depletion of the biocatalytic cascade and the recovery of the rest reaction module are substantially enhanced. In addition, we note that the absorbance of $ABTS^{\bullet-}$ formed (after a time interval of 2 min) by the separated constituents A_1-GOx and A_2-HRP

[at time $t = 0$ and optical density (OD) = 0.028] is substantially lower than the absorbance of $ABTS^{\bullet-}$ (generated after 2 min) by the peak content of the transient constituent T_1/A_1-GOx+A_2-HRP (OD = 0.11; Fig. 2A, panel III). This fourfold enhancement in the concentration of $ABTS^{\bullet-}$ is attributed to the spatial proximity between GOx and HRP in the constituent T_1/A_1-GOx+A_2-HRP that enables effective communication between the enzymes and efficient operation of the biocatalytic cascade.

Furthermore, the nucleic acid framework–guided operation of the transient biocatalytic cascade allows the coupling of the transient cascade to secondary transient catalyzed transformations. This is exemplified in Fig. 2 (D and E) with the coupling of the transient GOx/HRP cascade to the catalyzed transient generation of chemiluminescence by the catalyzed oxidation of luminol by H_2O_2 generated by the GOx/HRP cascade. That is, the transient formation of the supramolecular complex T_1/A_1-GOx+A_2-HRP leads to the aerobic oxidation of glucose to gluconic acid and H_2O_2, and the resulting H_2O_2 catalyzes, in the presence of HRP, the oxidation of luminol while generating chemiluminescence (Fig. 1, inset Y). Figure 2D depicts the chemiluminescence spectra λ = 425 nm at different time intervals of the chemiluminescence system. Figure 2E shows the dissipative chemiluminescence intensities generated by the transient biocatalytic cascade.

Nucleic acid–triggered transient lactate dehydrogenase/nicotinamide adenine dinucleotide catalytic cascade

The successful control over the bioenzyme cascade by means of the dynamic nucleic acid framework was then followed by applying the transient network to operate an enzyme cofactor–mediated biocatalytic process (Fig. 3). The reaction module II consists of the duplex L_1/T_1; the enzyme, lactate dehydrogenase (LDH) tethered to the nucleic acid A_1, A_1-LDH; the cofactor, nicotinamide adenine dinucleotide (NAD^+) linked to the nucleic acid B_2, B_2-NAD^+; and the nicking enzyme, Nt.BbvCI. (For the synthesis of the single nucleic acid–modified biocatalysts and the evaluation of the purities of the DNA-enzyme hybrids, see figs. S10 to S12 and table S1.) Subjecting the reaction module II to the fuel strand L_1' results in the displacement of the duplex L_1/T_1 by forming L_1'/L_1 and releasing T_1. The released T_1 hybridizes with the biocatalytic units, A_1-LDH and B_2-NAD^+, to form the supramolecular enzyme/NAD^+ assembly where the proximity between the constituents allows the activation of the biocatalytic cascade, leading to the LDH-catalyzed reduction of NAD^+ to NADH (reduced form of NAD^+) with the concomitant oxidation of lactic acid to pyruvic acid (Fig. 3, inset Z). The formation of the duplex L_1'/L_1 yields, however, a pre-engineered nicking site in L_1' that is nicked by Nt.BbvCI to yield the fragmented strands that are separated off from the strand L_1, as waste products, resulting in the free strand L_1. The released L_1 displaces T_1 from the biocatalytic supramolecular complex T_1/A_1-LDH+B_2-NAD^+ since the duplex L_1/T_1 is energetically stabilized as compared to the supramolecular complex. This results in the separation of A_1-LDH and B_2-NAD^+ bridged structure and switching off the biocatalytic LDH/NAD^+ cascade while restoring the original reaction module. That is, the design of the appropriate energetic balance, where the overall energy gained by the L_1'-triggered formation of the L_1'/L_1 and the supramolecular complex T_1/A_1-LDH+B_2-NAD^+ guides the activation of the biocatalytic cascade, yet the nicking of the complex L_1'/L_1 depletes the stability gained by L_1'/L_1 driving the recovery of the energetically stabilized duplex L_1/T_1, leading to the transient formation and depletion of the biocatalytic reactive structure. The transient formation/depletion of the intermediate complex T_1/A_1-LDH+B_2-NAD^+ is experimentally probed by analyzing samples at time intervals of the dynamically L_1'-triggered network and probing the transient content of the complex T_1/A_1-LDH+B_2-NAD^+ through the lactate/LDH-catalyzed reduction of NADH. Since the concentrations of the transient intermediate T_1/A_1-LDH+B_2-NAD^+ are low, samples of the transient species are withdrawn at time intervals of the dissipative process, and these are reacted with methylene blue (MB^+) to probe the rate of reduction of MB^+ to leucomethylene blue (MBH) by following the depletion of the absorbance of MB^+. By treatment of A_1-LDH+B_2-NAD^+ with variable concentrations of T_1 and treating the different concentrations of T_1/A_1-LDH+B_2-NAD^+ with MB^+ (5 μM) and lactate (1 mM), the resulting rates of reduction of MB^+ to MBH were evaluated, and an appropriate calibration curve relating the

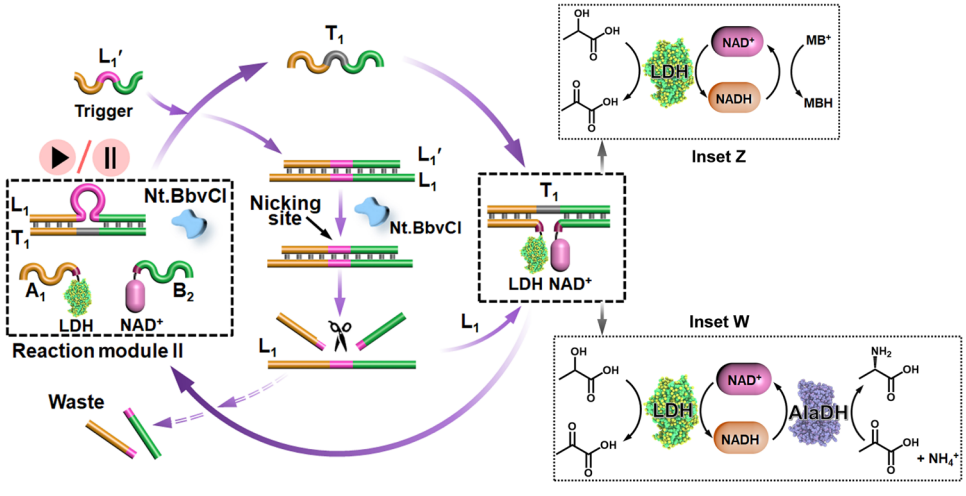

Fig. 3. Transient operation of the LDH/NAD^+ cascade. Schematic operation of the transient LDH/NAD^+ cascade driven by a nucleic acid hybridization/nicking machinery. Inset depicts the catalytic cycle to probe the transient formation of NADH using the NADH-stimulated reduction of MB^+ to the reduced colorless state MBH as optical probe (inset Z). The conjugation of the transient generation of NADH to the transient synthesis of alanine is depicted in inset W.

concentration of T_1/A_1-LDH+B_2-NAD^+ to the rate of MB^+ reduction was derived (fig. S13). The resulting calibration curve was then used to derive the transient concentration of the T_1/A_1-LDH+B_2-NAD^+.

Accordingly, to probe the L_1'-triggered activation of reaction module II to yield the transient biocatalytic intermediate, T_1/A_1-LDH+B_2-NAD^+ aliquots are taken out of the dynamic reaction mixture, and the temporal efficacy of biocatalytic intermediate associated with each aliquot was followed by the addition of lactic acid and MB^+ to each of the samples and following the time-dependent depletion of the absorbance of MB^+ (due to the formation of reduced MBH). Figure 4A depicts the time-dependent absorbance changes generated upon reduction of MB^+ by the T_1/A_1-LDH+B_2-NAD^+ intermediate species generated by the transient process (panels I and II), and the resulting transient absorbance change of MB^+ (after a fixed time interval of 2 min) are presented in panel III. Using an appropriate calibration curve relating the absorbance changes of MB^+ generated by defined concentrations of T_1/A_1-LDH+B_2-NAD^+ (fig. S13), the time-dependent transient absorbance changes shown in Fig. 4A (panel III) were translated into temporal molar concentrations of the transient, dissipative, catalytic intermediate T_1/A_1-LDH+B_2-NAD^+. Figure 4B [curve (i_a)] shows the transient concentrations of T_1/A_1-LDH+B_2-NAD^+ generated by the reaction module I shown in Fig. 3, in the presence of L_1' (6 μM) and the nicking enzyme (0.046 μM). The transient network–driven cascade was computationally simulated (see kinetic model in fig. S14), and the kinetic parameters of the best fit transient curve (i_a') are tabulated in table S3. These rate constants were used to predict the transient behavior of the system at different auxiliary conditions: L_1' = 3 μM, Fig. 4B [curve (i_b')]; nicking enzyme = 0.0307 μM, Fig. 4C [curve (i_c')]; and nicking enzyme = 0.0765 μM, Fig. 4C [curve (i_d')]. Note that the time-dependent absorbance changes of $ABTS^{\bullet-}$ at the auxiliary parameters to drive the transient curves corresponding to curves (i_b-i_d) in Fig. 2 (B and C) are presented in fig. S15. The computationally predicted results were experimentally validated [curve (i_b-i_d) in Fig. 4 (B and C)]. The experimental results fit well with the predicted transient systems. The decrease in the concentration of L_1' reduces the peak content of the biocatalytic cascade and enhances the depletion of the biocatalytic process. The increase in the concentration of the nicking enzyme decreases the peak content of supramolecular complex and enhances the depletion of the transient process.

In addition, the dissipative, transient formation of the T_1/A_1-LDH+B_2-NAD^+ intermediate was conjugated to the secondary transient NADH-mediated synthesis of alanine [Figs. 3 (inset W) and 4D]. In this experiment, the reaction module II was subjected to the trigger L_1', in the presence of alanine dehydrogenase (AlaDH). Under these conditions, the transient LDH–catalyzed generation of NADH yields concomitantly pyruvic acid. The generated pyruvic acid undergoes, in the presence of the formed NADH, AlaDH, and NH_4^+ presenting in the buffer solution, the reductive amination of pyruvic acid to form alanine. The resulting alanine was analyzed by mass spectrometry, and using an appropriate calibration curve (table S4 and fig. S16), the transient formation of alanine, at time

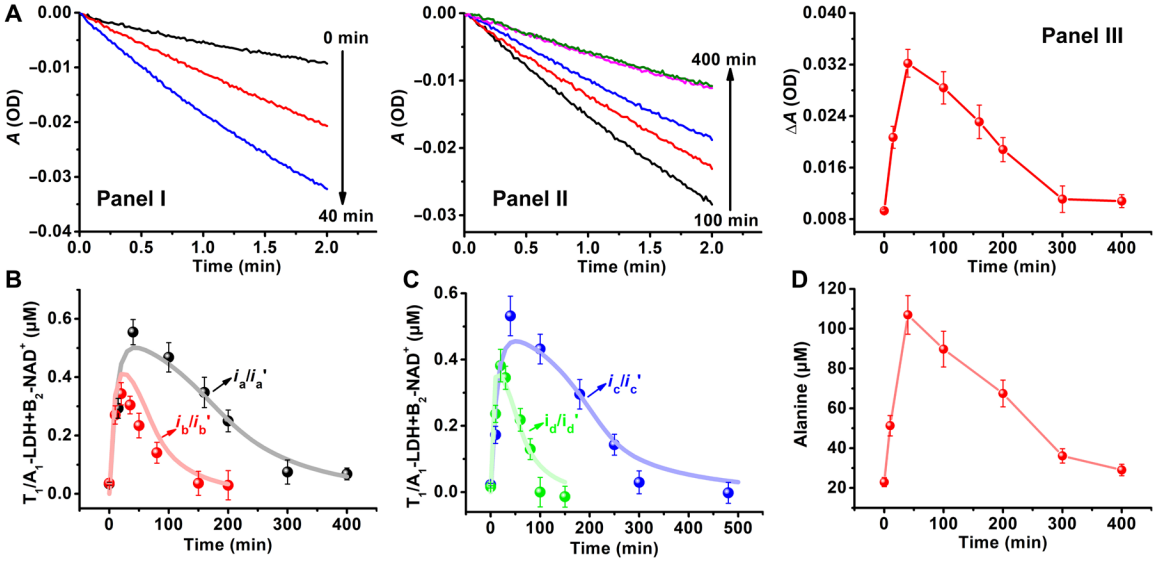

Fig. 4. Transient curves associated with the LDH/NAD^+ cascade. (**A**) Panel I and II: Time-dependent absorbance changes (λ = 630 nm) upon reduction of MB^+ to MBH by T_1/A_1-LDH+B_2-NAD^+ generated by reaction module II (Fig. 3). Conditions: T_1, L_1, A_1-LDH, and B_2-NAD^+ = 1 μM; Nt.BbvCI = 0.046 μM; and L_1' = 6 μM. Panel III: Transient absorbance changes of MB^+ after a time interval of 2 min. By applying a calibration curve relating the absorbance of MB^+ generated (after a time interval of 2 min) in the presence of variable concentrations of T_1/A_1-LDH+B_2-NAD^+, the transient concentrations of T_1/A_1-LDH+B_2-NAD^+ generated by reaction module II were evaluated. (**B**) Solid dots, curve (i_a): Transient concentrations of T_1/A_1-LDH+B_2-NAD^+ catalyzing the LDH reduction of NAD^+ by lactate formed by the L_1'-triggered module II (Fig. 3). Conditions: T_1, L_1, A_1-LDH, and B_2-NAD^+ = 1 μM; Nt.BbvCI = 0.046 μM; and L_1' = 6 μM. Solid curve (i_a'): Computationally simulated curve of experimental transient (i_a), using the kinetic (fig. S14). Solid curve (i_b'): Computationally predicted transient formation/depletion of complex T_1/A_1-LDH+B_2-NAD^+ under L_1' = 3 μM using the rate constants tabulated in table S3, derived from simulations of curves (i_a)/(i_a'). Solid dots (i_b) experimentally validated results. (**C**) Curves (i_c') and (i_d') predicted transients of constituent T_1/A_1-LDH+B_2-NAD^+ in the presence of Nt.BbvCI (0.0307 and 0.0765 μM) using the rate constants derived from (i_a)/(i_a'). Curves (i_c) and (i_d): Experimental validation of the predicted transients at the specified conditions. T_1, L_1, A_1-LDH, and B_2-NAD^+ = 1 μM and L_1' = 6 μM. (**D**) Transient formation of alanine by the temporal reductive amination of the T_1/A_1-LDH+B_2-NAD^+–generated pyruvate in the presence of added AlaDH (80 U ml^{-1}) and NH_4^+ (1 mM). Error bars are derived from N = 3 experiments.

intervals of the dissipative formation of the intermediary T_1/A_1-LDH+B_2-NAD^+ cascade, was evaluated (Fig. 4D).

Note that we made use of 3′-thiolated strand A_1 and 5′-thiolated strand A_2 to modify the GOx and HRP backbone at single-point sites in the reaction module I (operating the GOx/HRP cascade). For the reaction module II, we made use of 3′-thiolated strand A_1 to modify the LDH at single-point sites and 5′-amino–modified strand B_2 to functionalize NAD^+ through the boronic acid ligand (fig. S1). The base sequence in the strands A_2 and B_2 are, however, identical.

Nucleic acid–driven gated transient biocatalytic cascades

The successful operation of two different biocatalytic cascades using the same reaction module consisting of the L_1/T_1, the nicking enzyme Nt.BbvCI, and the triggering input L_1', suggests that the two biocatalytic cascades could be activated in parallel by the reaction module and eventually, by appropriate design of the reaction module, could be operated as a gated and selective biocatalyst transient system. This is exemplified in Fig. 5 with the design of a reaction module, state X, consisting of L_1/T_1, the nicking enzyme, and the mixture of constituent pairs C_1-GOx/C_2-HRP; D_1-LDH/D_2-NAD^+. Note that to operate the parallel (or gated) biocatalytic cascades consisting of the GOx/HRP and LDH/NAD^+ cascades, we had to re-engineer the nucleic acids C_1, C_2, D_1, and D_2 functionalizing the biocatalysts GOx, HRP, LDH, and NAD^+, respectively. (For the characterization of single strand–modified enzyme and cofactor, see figs. S17 to S20.) As stated, vide supra, the original tethers used in reaction modules I and II include in the nucleic acid strand identical sequences. Thus, to eliminate perturbing cross-talks between the constituents involved in the system, the original sequences A_1 and A_2 were elongated with the complementary sequences x and x', respectively, to yield C_1 and C_2, and the strands A_1 and B_2 were elongated with the complementary sequences y and y' to yield the strands D_1 and D_2, respectively (Fig. 5, state X). Under this re-engineering of the strands, the guided selective formation of the T_1/C_1-GOx+C_2-HRP and T_1/D_1-LDH+D_2-NAD^+ complexes in state X proceeds. Triggering the reaction module in state X with L′ results in the parallel transient operation of the two biocatalytic cascades GOx/HRP and LDH/NAD^+. Treatment of the reaction module in state X with the inhibitor I_C results in the hybridization of I_C with C_2-HRP and the formation of the reaction module in state Y. Triggering state Y with the fuel strand L_1' activates the transient operation of the LDH/NAD^+ module, while the biocatalytic GOx/HRP cascade is switched off. Subjecting the reaction module in state X to the inhibitor I_D results in the hybridization of I_D to constituent D_2-NAD^+, forming the reaction module in state Z. In the presence of the triggering fuel L_1', the transient GOx/HRP biocatalytic cascade is activated, while the LDH/NAD^+ cascade is switched off. That is, by applying the inhibitors I_C or I_D, the gated operation of the respective biocatalytic cascades is anticipated to proceed.

Figure S22 (A and B) presents the experimental data corresponding to the absorbance changes associated with the products generated by the inhibitor-guided transient GOx/HRP and LDH/NAD^+ cascades. Figure S22A depicts the transient absorbance changes of the $ABTS^{\bullet-}$ associated with the GOx/HRP cascade in panel I and the absorbance changes of MB^+ associated with the LDH/NAD^+ cascade [panel II, in the absence of the inhibitor I_C curves (i_a)] and upon elevating the concentration of the inhibitor I_C, curves (i_b) and (i_c), respectively. In the absence of the inhibitor, the transient products of the two cascades are observed, yet at an I_C concentration of 1 μM,

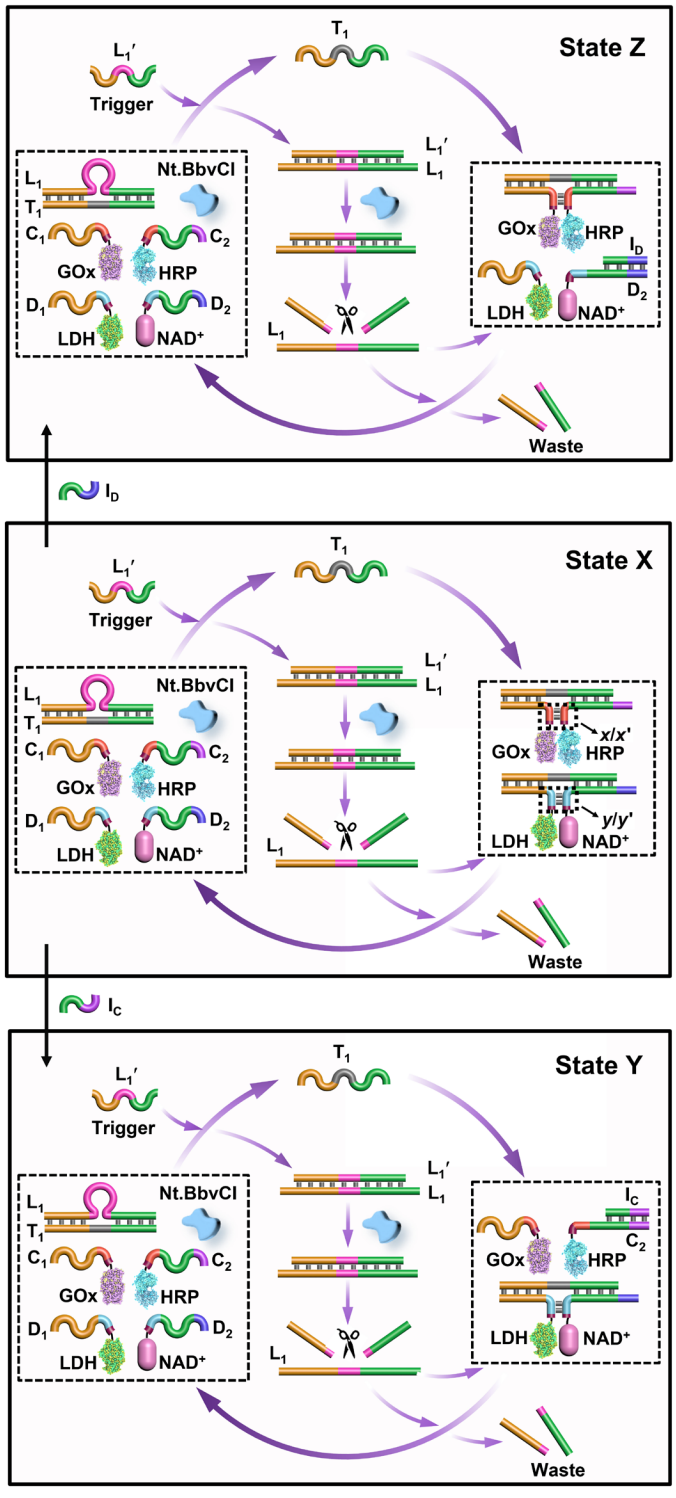

Fig. 5. Gated operation of nucleic acid–guided transient biocatalytic cascades. Scheme for the inhibitor-guided gating of transient biocatalytic cascades. The reaction model in state X activates the L_1'-triggered simultaneous operation of the two biocatalytic cascades consisting of GOx/HRP and LDH/NAD^+. In the presence of inhibitor I_C, the GOx/HRP cascade is blocked (inhibited) (state Y), giving rise to the selective gated LDH/NAD^+ cascade. In the presence of inhibitor I_D, the LDH/NAD^+ cascade is blocked (state Z), leading to the selective gated operation of the GOx/HRP cascade.

the product of the GOx/HRP cascade is almost fully blocked [panel I, curve (i_c)], whereas the LDH/NAD$^+$ cascade product is intensified [panel II, curve (i_c)]. Similarly, fig. S22B demonstrates the effects of the I_D-guided gated absorbance changes of the products generated by the two cascades. While the transient catalytic formation of the products associated with the two cascades are observed in the absence of I_D [panels I and II, curves (i_a)], at concentration of I_D corresponding to 1 μM, the product generated by the LDH/NAD$^+$ cascade is almost fully blocked [panel II, curve (i_c)], and the transient absorbance changes associated with the products of the GOx/HRP cascade are intensified. The calibration curves corresponding to the relation between the absorbance changes of the biocatalytic products associated with the GOx/HRP and LDH/NAD$^+$ cascades and the concentrations of the transient intermediate catalytic complexes driving these cascades, e.g., T_1/C_1-GOx+C_2-HRP and T_1/D_1-LDH+D_2-NAD$^+$, are presented in figs. S23 and S24. Accordingly, Fig. 6 displays the effect of inhibitor-guided transient concentration changes of the catalytic intermediates driving the GOx/HRP and LDH/NAD$^+$ cascades. Figure 6A [panels I and II, curves (i_a)] displays the transient concentrations of the catalytically active intermediates driving the nongated GOx/HRP and LDH/NAD$^+$ cascades. Subjecting the reaction module in state X to the inhibitor I_C transforms the state X to state Y where the gated catalytic operation of the LDH/NAD$^+$ cascade proceeds. As the concentration of I_C increases, the inhibition of the GOx/HRP cascade is enhanced. At a concentration of I_C = 1 μM, the concentration of the catalytically active intermediate operating the GOx/HRP cascade is, almost, fully blocked, resulting in the increased transient concentration of the catalytic intermediate T_1/D_1-LDH+D_2-NAD$^+$ that guides the transient LDH/NAD$^+$ cascade [Fig. 6A, panels I and II, curve (i_c)]. Similarly, treatment of the module in state X with the inhibitor I_D results in the transition of state X into state Z where the inhibition of the transient intermediate T_1/D_1-LDH+D_2-NAD$^+$ proceeds while the biocatalytic transient intermediate T_1/C_1-GOx+C_2-HRP guiding the GOx/HRP cascades operates effectively (Fig. 6B). While the two biocatalytic intermediate are nongated and operate concomitantly in the absence of I_D, the inhibitor I_D blocks the intermediates T_1/D_1-LDH+D_2-NAD$^+$ while enhancing the intermediate driving the GOx/HRP cascade. At I_D = 1 μM, the formation of the catalytic intermediate operating the LDH/NAD$^+$ cascade is almost totally blocked, while the concentration of the intermediate driving the transient GOx/HRP cascade increases [Fig. 6B, panels I and II, curves (i_c)]. The parallel operation of the two transient biocatalytic processes using the newly designed reaction module in state X and the gated operation of the biocatalytic cascades were further computationally simulated. The kinetic model formulated in fig. S25 accounts for the parallel operation of the two biocatalytic cascades in the absence of the inhibitors (state X). The tilted simulated results are overlaid as curves (i_a') (solid curves) on the experimental transient curves (solid points) [Fig. 6A, curve (i_a)] for the transient GOx/HRP cascade (panel I) and LDH/NAD$^+$ cascade (panel II). The desired simulated rated constants are summarized in table S5. The inhibitor I_C–gated operation of reaction module state Y was simulated following the kinetic module presented in fig. S26 using the experimental results in the presence of I_C = 0.5 μM. The titled simulated curves (i_b') for the GOx/HRP cascade and the LDH/NAD$^+$ cascade (solid curves) are overlaid on the experimental transients (solid points) presented in Fig. 6A [curves (i_b) in panels I and II, respectively]. The derived simulated rate constants are summarized

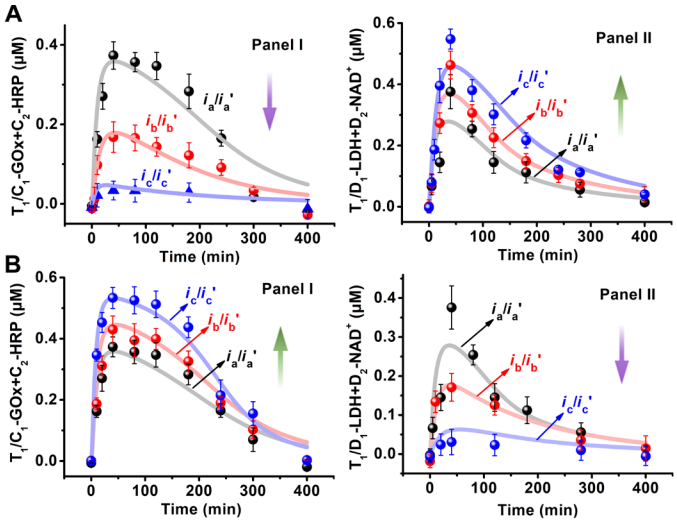

Fig. 6. Dynamic curves associated with the gated, transient operation of biocatalytic cascades. Inhibitor-guided, gated, transient curves corresponding to the GOx/HRP and LDH/NAD$^+$ biocatalytic cascades in the presence of different concentrations of the inhibitors I_C or I_D applied on the reaction module in state X: (**A**) Gated activation of the LDH/NAD$^+$ cascade upon subject state X to the trigger L_1' at variable concentrations of I_C (state Y). Panel I: The transient GOx/HRP biocatalytic cascade in the absence of I_C [curves (i_a)/(i_a')] and in the presence of 0.5 μM I_C [curves (i_b)/(i_b')] and 1 μM I_C [curves (i_c)/(i_c')]. Panel II: The transient LDH/NAD$^+$ cascade in the absence of I_C [curves (i_a)/(i_a')] and in the presence of 0.5 μM I_C [curves (i_b)/(i_b')] and 1 μM I_C [curves (i_c)/(i_c')]. Curves (i_a-i_c) correspond to experimental results, and curves (i_a'-i_c') correspond to fitting results. Note that increasing concentration of I_C result in the blocking the GOx/HRP cascade and the enhancement of LDH/NAD$^+$ cascade. (**B**) Gated activation of the GOx/HRP cascade upon subjecting state X to the trigger L_1' at variable concentrations of I_D (state Z). Panel I: The transient GOx/HRP biocatalytic cascade in the absence of I_D [curves (i_a)/(i_a')] and in the presence of 0.5 μM I_D [curves (i_b)/(i_b')] and 1 μM I_D [curves (i_c)/(i_c')]. Panel II: The transient LDH/NAD$^+$ cascade in the absence of I_D [curves (i_a)/(i_a')] and in the presence of 0.5 μM I_D [curves (i_b)/(i_b')] and 1 μM I_D [curves (i_c)/(i_c')]. Curves (i_a-i_c) correspond to experimental results, and curves (i_c)/(i_c') correspond to fitting results. Note that increasing concentration of I_D result in the blocking the LDH/NAD$^+$ cascade and the enhancement of GOx/HRP cascade. The simulated results presented in the respective transients curves (i_a')/(i_b')/(i_c') are explained in the text. Error bars are derived from N = 3 experiments.

in table S6. These rate constants were used to predict the gating effect in the presence of I_C = 1 μM, and the results are presented in curves (i_c)/(i_c') for the GOx/HRP and LDH/NAD$^+$ cascades (Fig. 6A, panels I and II). Similarly, the I_D inhibitor–gated reaction module shown in Fig. 5 (state Z) was computationally simulated, following the kinetic model formulated in fig. S27. The simulated kinetic curves corresponding to the biocatalytic cascades GOx/HRP and LDH/NAD$^+$ in the presence of I_D = 0.5 μM are presented in Fig. 6B [curves (i_b'); panel I for GOx/HRP and panel II for LDH/NAD$^+$] overlaid on the respective experimental curve (i_b). The derived rate constants are summarized in table S7. The derived rate constants were used to predict the transient curves of the GOx/HRP and LDH/NAD$^+$ in the presence of I_D = 1 μM, and these are presented as solid curves (i_c') in Fig. 6B [panel I (for GOx/HRP cascade) and panel II (for LDH/NAD$^+$ cascade)], overlaid on the respective experimental transient [Fig. 6B, curve (i_c')]. The gated biocatalytic cascade described in Fig. 6 represents static effects of the inhibitors on the mixture of the two transient biocatalytic cascades. That is,

the inhibitors were added and equilibrated with the mixture of the two biocatalytic reaction modules, and the triggered gated operation was monitored on the static inhibitor-equilibrated systems. One may, however, probe the dynamic effect of the inhibitor on the transient operation of the two reaction modules operating in parallel. That is, the L_1'-triggered operation of the two transient biocatalytic reaction modules is initiated in parallel, and after a defined time interval, the inhibitor is added to the system and the dynamic effect of the inhibitor on the two parallelly operating processes is probed. The results of such experiment are presented and discussed in fig. S28.

DISCUSSION

The study emulated native transient networks guiding biocatalytic cascades by introducing artificial nucleic acid networks that control transient biocatalytic cascaded and dynamically triggered gated biocatalytic cascades. Specifically, the transient operations of the GOx/HRP cascade and of the LDH/NAD^+ cascade were demonstrated, and the dynamic gated, transient operation of the mixture of biocatalytic cascades was accomplished through the spatiotemporal control over sterically confined structures of supramolecular biocatalytic complexes. Besides, the experimental design of the dynamic networks was computationally simulated using appropriate kinetic models. The computational simulations allowed us to predict and experimentally validate the behavior of the systems under different auxiliary parameters.

Beyond the significance of the systems providing dynamic models emulating transient biologically triggered processes (Systems Chemistry), such networks could be important by introducing new concepts to the areas of chemical synthesis and dynamic medical applications. For example, the transient, dissipative, network-driven synthesis of NADH could be coupled to secondary biocatalytic transformations, such as the synthesis of amino acids. Similarly, the enzyme-driven transient, biocatalytic cascades could have therapeutic applications, such as the temporal intracellular control of biologically active ingredient such as signaling agents or transient control over blood clotting agents, e.g., thrombin, the temporal intracellular in body fluid dose release of drugs or the dose-controlled formation of reactive oxygen species for therapeutic applications. For example, dopamine acts as a versatile neurotransmitter that activates different neural networks (*63*). Accordingly, we applied the transient GOx/HRP cascade as a functional scaffold that temporally controls the transient depletion of dopamine as a model for possible control of neurotransmitter concentrations and neural responses. The results are presented in fig. S29 and accompanying discussion. In addition, the dynamic networks are, at present, operating in homogeneous environments. Their integration in cell-like containments, such as vesicles, polymersomes, dendrosomes, or microcapsules, could provide protocell carriers for permeation into cellular organs and versatile means to intervene with cellular processes.

MATERIALS AND METHODS

Materials

GOx from *Aspergillus niger* (187300 U g^{-1}), HRP type II (219,000 U g^{-1}), NAD^+, succinimidyl 3-(2-pyridyldithio)propionate (SPDP), 4-carboxyphenylboronic acid, 1-ethyl-3-(3-dimethylaminopropyl) carbodiimide (EDC), *N*-hydroxysulfosuccinimide (NHS), LDH from rabbit muscle (550 U mg^{-1}), AlaDH [recombinant, expressed in *Escherichia coli* (21 U mg^{-1})], pyruvic acid, glucose, $ABTS^{2-}$, dopamine, MB^+, hydrazine hydrate, and ethanol were purchased from Sigma-Aldrich. Nucleic acid strands were purchased from Integrated DNA Technologies Inc. (Coralville, IA). NEBuffer 2.1 Buffer was purchased from New England BioLabs Inc. DNA oligonucleotides were purchased from Integrated DNA Technologies Inc. The nucleic acid sequences used in the study include the following: T_1, 5′-GGTTTGTGATGGACGTTCTTCTGTC-3′; L_1, 5′-GACAGAAGAACGCTGAGGCCATCACAAACC-3′; L_1', 5′-GATGGCCTCAGCGTT-3′; A_1, 5′-TTTTTTTTTTTTTTACAGAAGAACCTCGAC-SH-3′; A_2, 5′-SH-TTTTTTCCATCACAAA AACTTTTTTTTTTTTTT-3′; B_2, 5′-NH_2-TTTTTTCCATCACAAAAACTTTTTTTTTTTTT-3′; B_2', 5′-NH_2-TTTTTTCCATCACAAAAACTTTTTTTTTTTTT-Cy3-3′; C_1, 5′-TTTTTTTTTTACAGAAGAACCTCGACTTT-SH-3′; C_2, 5′-SH-TTTGTCGAGCCATCACAAA AATTTCACCCATG-3′; D_1, 5′-TTTTTTTTTTACAGAAGAACCGGCTGTTT-SH-3′; D_2, 5′-NH_2-TTTCAGCCGCCATCACAAAGGAAAGAGGCAGG-3′; D_2', 5′-NH_2-TTTCAGCCGCCATCACAAAGGAAAGAGGCAGG-Cy3-3′; I_C, 5′-CATGGGTGAAATTTTTG-3′; I_D, 5′-CCTGCCTCTTTCCTTTG-3′; F_1, 5′-Cy5-TCGTCCTCAGCT-3′; and Q_1, 5′-AGCTGAGGACGA-BHQ2-3′.

Instrumentation

Absorption spectra were recorded at 25°C using a UV-2450 spectrophotometer (Shimadzu), and a cuvette of 50-μl volume (made of Quartz SUPRASIL; Hellma Analytics) was used in these experiments. Fluorescence spectra were recorded at 25°C using a Cary Eclipse Fluorometer (Varian Inc.), and a cuvette of 100-μl volume (disposable cuvettes; Brand GmbH, Wehrheim, Germany) was used in these experiments. Mass analysis was obtained by liquid chromatography–mass spectroscopy LC(UV)MS using Agilent 6520 QTOF analyzer. Mass data were collected using Mass Hunter Workstation software 6.00. The data were analyzed using Mass Hunter Quantitative Analysis B.06.00. In positive mode, the mobile phase is 0.01% aqueous formic acid:H_2O = 1:1, and glycine was used as an internal standard.

Methods

Modification of strand A_1 or C_1 with GOx

GOx (80 μl, 100 μM) reacted with SPDP (2.4 μl, 0.01 M) in HEPES buffer (10 mM, pH 7.2) for 1 hour. Amicon 10-kDa-cutoff filters were used to wash out excess SPDP three times. Then, strand A_1 or C_1 (eightfold excess) was conjugated to SPDP-modified GOx through a disulfide bond exchange of the activated pyridyldithiol group. The reaction mixture was shaken in HEPES buffer (10 mM, pH 7.2) for 2 hours. The release of pyridine-2-thione (extinction coefficient, 8080 M^{-1} cm^{-1}, 343 nm) after strand conjugated to enzyme is probed for evaluating the coupling efficiency (figs. S2A and S17A). Last, the excess DNA was removed by washing with Amicon 30-kDa-cutoff filters. The ratio of enzyme and DNA can be also quantified by measuring the absorbance at 260 and 280 nm (figs. S2B and S17B and table S1). The enzymatic activity of the DNA-modified GOx was ~77% of the activity of the native enzyme (figs. S2C and S17C).

Modification of strand A_2 or C_2 with HRP

HRP (80 μl, 100 μM) reacted with SPDP (5.6 μl, 0.01 M) in HEPES buffer (10 mM, pH 7.2) for 1 hour. Amicon 10-kDa-cutoff filters were used to wash out excess SPDP three times. Then, strand A_2 or C_2

(eightfold excess) was conjugated to SPDP-modified HRP through a disulfide bond exchange of the activated pyridyldithiol group. The reaction mixture was shaken in HEPES buffer (10 mM, pH 7.2) for 2 hours. The release of pyridine-2-thione (extinction coefficient, 8080 M^{-1} cm^{-1}, 343 nm) after strand conjugated to enzyme is probed for evaluating the coupling efficiency (figs. S3A and S18A). Last, the excess DNA was removed by washing with Amicon 30-kDa-cutoff filters. The ratio of enzyme and DNA can be also quantified by measuring the absorbance at 260 and 280 nm (figs. S3B and S18B and table S1). The enzymatic activity of the DNA-modified HRP was ~82% of the activity of the native enzyme (figs. S3C and S18C).

Modification of strand A_1 or D_1 with LDH

LDH (100 μl, 23 μM) reacted with SPDP (4 μl, 0.5 M) in HEPES buffer (10 mM, pH 7.2) for 1 hour. Amicon 10-kDa-cutoff filters were used to wash out excess SPDP three times. Then, strand A_1 or D_1 (eightfold excess) was conjugated to SPDP-modified LDH through a disulfide bond exchange of the activated pyridyldithiol group. The reaction mixture was stirred in HEPES buffer (10 mM, pH 7.2) for 2 hours. The release of pyridine-2-thione (extinction coefficient, 8080 M^{-1} cm^{-1}, 343 nm) after strand conjugated to enzyme is probed for evaluating the coupling efficiency (figs. S10, A and B, and S19, A and B). Last, the excess DNA was removed by washing with Amicon 30-kDa-cutoff filters. The ratio of enzyme and DNA can be also quantified by measuring the absorbance at 260 and 280 nm (figs. S10C and S19C and table S1). The enzymatic activity of the DNA-modified LDH was ~82% of the activity of the native enzyme (figs. S10D and S19D).

Modification of strand B_2 or D_2 with NAD^+

The schematic preparation of B_2- or D_2-NAD^+ was shown in fig. S1. 4-Carboxyphenylboronic acid (2 μl, 50 mM) reacted with EDC (3 μl, 10 mg ml^{-1}) in 200 μl of MES buffer (10 mM, pH 5.5) for 5 min. Subsequently, NHS (5 μl, 10 mg ml^{-1}) in 200 μl of phosphate buffer (PB) (50 mM, pH 7.2) was added and reacted for 10 min; then, strand B_2 or D_2 (10 μl, 1 mM) was reacted with the reaction mixture for 2 to 3 hours. Excess undesired molecules were removed by washing three times with Amicon 3-kDa-cutoff filters. Last, the resulting solution reacted with NAD^+ (10 μl, 10 mM) in PB buffer (50 mM, pH 10) for 2 hours under room temperature and overnight under 4°C. The products of B_2- or D_2-NAD^+ were obtained by washing with Amicon 3-kDa-cutoff filters several times. For the characterization of the single nucleic acid–modified cofactor, see figs. S11, S12, and S20 and table S1.

The purity of the single nucleic acid–modified enzymes was further confirmed by gel electrophoretic experiment (agarose gel, 3%; fig. S21). The separation process was conducted in 1× tris-borate EDTA buffer under 100 V for time interval of 3 hours.

Dissipative control over the GOx/HRP cascade by DNA networks

By subjecting rest configuration of the system consisting of A_1-GOx, A_2-HRP, T_1, and L_1 (1 μM) to a 1× CutSmart buffer [50 mM potassium acetate, 20 mM tris-acetate, 10 mM magnesium acetate, and bovine serum albumin (BSA; 100 μg ml^{-1}; pH 7.9) at 25°C], the mixture was incubated at 45°C and then cooled down to 25°C at a rate of 0.33°C min^{-1}. The prepared mixture was subjected to the different concentrations of nicking enzyme, Nt.BbvCI, and then, the resulting mixture was transferred into the tubes. Note that the nicking enzyme of buffer exchange process was achieved by washing with 30-kDa Amicon filter several times, and a calibration curve was used for quantifying the concentration of nicking enzyme (fig. S4). The commercially supplied Nt.BbvCI includes dithiothreitol as stabilizer. Its removal from the reaction mixtures is essential since the modification of the enzymes with the nucleic acid tethers includes an S-S bridge. The dithiothreitol additive degrades the disulfide bridge, and hence, its removal is essential for all the dissipative system. The variable concentrations of fuel strands L_1' were added to the mixture. Subjecting the aliquots of the L_1'-triggered dissipative system to 40 μM glucose and 100 μM $ABTS^{2-}$ with different time intervals allows us to probe activation of the GOx/HRP cascade by the time-dependent absorbance of oxidation of $ABTS^{\bullet-}$ at λ = 420 nm (probing for 2 min). The transient biocatalytic cascade allows the coupling of the transient cascade to secondary transient catalyzed transformations by subjecting the aliquots of L_1'-triggered dissipative system to 5 mM glucose and 500 μM luminol at different time intervals. The signal readout was measured by the chemiluminescent spectra of oxidized luminol. The transient biocatalytic cascade allows the coupling of the transient cascade to transient catalyzed transformations by subjecting the L_1'-triggered aliquots of dissipative system to 50 μM glucose and 50 μM dopamine. The signal readout was measured by the absorbance of oxidation of dopamine at λ = 480 nm (probing for 2 min).

Dissipative control over the LDH/NAD^+ cascade by DNA networks

By subjecting rest configuration of the system consisting of A_1-LDH, B_2-NAD^+, T_1, and L_1 (1 μM) to a 1× CutSmart buffer [50 mM potassium acetate, 20 mM tris-acetate, 10 mM magnesium acetate, and BSA (100 μg ml^{-1}; pH 7.9) at 25°C], the mixture was incubated at 45°C and then cooled down to 25°C at a rate of 0.33°C min^{-1}. The prepared mixture was subjected to the different concentrations of nicking enzyme, Nt.BbvCI, and then, the resulting mixture was transferred into the tubes. The variable concentrations of fuel strands L_1' were added to the mixture. Subjecting the aliquots of the L_1'-triggered dissipative system to 1 mM lactic acid, 1 mM hydrazine, and 50 μM MB^+ with different time intervals allows us to probe activation of the LDH/NAD^+ cascade by the time-dependent absorbance of reduction of MB^+ at λ = 630 nm (probing for 2 min).

The transient biocatalytic cascade allows the coupling of the transient cascade to metabolic transformations by subjecting the aliquots of L_1'-triggered dissipative system to 1 mM lactic acid, 1 mM hydrazine, 1 mM NH_4Cl, 0.8 mM glycine, and AlaDH (80 U ml^{-1}) with different time intervals. The alanine was generated and probed by performing mass analysis at positive mode with glycine as internal standard. The amount of generated alanine was calculated on the basis of the integrated area ratio between mass/charge ratio (m/z) = 90 (alanine) and m/z = 76 (glycine). The integrated area values of different mass peaks under dissipative process were summarized in table S4.

Dissipative control over the gated bioenzyme cascade by DNA networks

By subjecting rest configuration of the system consisting of C_1-GOx, C_2-HRP, D_1-LDH, D_2-NAD^+, T_1, L_1 (1 μM), and Nt.BbvCI (0.046 μM) to a 1× CutSmart buffer [50 mM potassium acetate, 20 mM tris-acetate, 10 mM magnesium acetate, and BSA (100 μg ml^{-1}; pH 7.9) at 25°C], the mixture was incubated at 45°C and then cooled down to 25°C at a rate of 0.33°C min^{-1}. The variable concentrations of fuel strands L_1' and inhibitors were added to the mixture. The transformations of $ABTS^{2-}$ to $ABTS^{\bullet-}$ and MB^+ to MBH were followed by the same procedure of GOx/HRP and LDH/NAD^+ parts.

Subjecting the aliquots of gated dissipative system to 40 μM glucose and 100 μM $ABTS^{2-}$ with different time intervals allows us to probe activation of the GOx/HRP cascade by the time-dependent absorbance of oxidation of $ABTS^{\bullet-}$ at λ = 420 nm (probing for 2 min). Subjecting the aliquots of gated dissipative system to 1 mM lactic acid, 1 mM hydrazine, and 50 μM MB^+ with different time intervals allows us to probe activation of the LDH/NAD^+ cascade by the time-dependent absorbance of reduction of MB^+ at λ = 630 nm (probing for 2 min).

Computational kinetic simulations of the systems

Kinetic models for each of the transient catalytic systems described in the study were formulated. The set of rate constants associated with the optimized filled curves were evaluated. To support the derived rate constants as a meaningful representative solution for the system (rather than a coincidental local solution), several steps were undertaken:

1) The set of rate constants being common in the different simulated schemes was adjusted to represent a global set of values that represents consistently the simulations of all systems.

2) The derived rate constants were used to predict the transient behavior, and auxiliary conditions were not used to derive the simulated rate constants; the predicted transient behavior was defined. These predictions were then evaluated by experiments. The experimental results were in good agreement with the predictions.

3) Whenever possible, a set of rate constants being a part of the kinetic mode that can be experimentally evaluated was selected. These rate constants were experimentally tested and compared to the simulated results. Specifically, in the present study, k_2 and k_{-2} for the kinetic model formulated in fig. S6 were experimentally evaluated (fig. S7). The experimental values, k_2 = 0.47 μM^{-1} min^{-1} and $k_{-2} = 10.9\,\mu M^{-1}\,min^{-1}$, fit well the simulated values $k_2 = 0.54\,\mu M^{-1}\,min^{-1}$ and k_{-2} = 11.3 μM^{-1} min^{-1}.

SUPPLEMENTARY MATERIALS

Supplementary material for this article is available at https://science.org/doi/10.1126/sciadv.abn3534

View/request a protocol for this paper from *Bio-protocol*.

REFERENCES AND NOTES

1. G. Ashkenasy, T. M. Hermans, S. Otto, A. F. Taylor, Systems chemistry. *Chem. Soc. Rev.* **46**, 2543–2554 (2017).
2. E. Mattia, S. Otto, Supramolecular systems chemistry. *Nat. Nanotechnol.* **10**, 111–119 (2015).
3. R. Merindol, A. Walther, Materials learning from life: Concepts for active, adaptive and autonomous molecular systems. *Chem. Soc. Rev.* **46**, 5588–5619 (2017).
4. L. Rothfield, A. Taghbalout, Y. L. Shih, Spatial control of bacterial division-site placement. *Nat. Rev. Microbiol.* **3**, 959–968 (2005).
5. B. Bugyi, M. F. Carlier, Control of actin filament treadmilling in cell motility. *Annu. Rev. Biophys.* **39**, 449–470 (2010).
6. J. Boekhoven, W. E. Hendriksen, G. J. Koper, R. Eelkema, J. H. van Esch, Transient assembly of active materials fueled by a chemical reaction. *Science* **349**, 1075–1079 (2015).
7. M. Tena-Solsona, C. Wanzke, B. Riess, A. R. Bausch, J. Boekhoven, Self-selection of dissipative assemblies driven by primitive chemical reaction networks. *Nat. Commun.* **9**, 2044 (2018).
8. R. S. M. Rikken, H. Engelkamp, R. J. M. Nolte, J. C. Maan, J. C. M. Van Hest, D. A. Wilson, P. C. M. Christianen, Shaping polymersomes into predictable morphologies via out-of-equilibrium self-assembly. *Nat. Commun.* **7**, 12606 (2016).
9. A. Sorrenti, J. Leira-Iglesias, A. J. Markvoort, T. F. A. de Greef, T. M. Hermans, Non-equilibrium supramolecular polymerization. *Chem. Soc. Rev.* **46**, 5476–5490 (2017).
10. S. A. P. van Rossum, M. Tena-Solsona, J. H. van Esch, R. Eelkema, J. Boekhoven, Dissipative out-of-equilibrium assembly of man-made supramolecular materials. *Chem. Soc. Rev.* **46**, 5519–5535 (2017).
11. J. H. van Esch, R. Klajn, S. Otto, Chemical systems out of equilibrium. *Chem. Soc. Rev.* **46**, 5474–5475 (2017).
12. H. Hess, J. L. Ross, Non-equilibrium assembly of microtubules: From molecules to autonomous chemical robots. *Chem. Soc. Rev.* **46**, 5570–5587 (2017).
13. S. Bal, K. Das, S. Ahmed, D. Das, Chemically fueled dissipative self-assembly that exploits cooperative catalysis. *Angew. Chem. Int. Ed. Engl.* **58**, 244–247 (2019).
14. L. S. Kariyawasam, C. S. Hartley, Dissipative assembly of aqueous carboxylic acid anhydrides fueled by carbodiimides. *J. Am. Chem. Soc.* **139**, 11949–11955 (2017).
15. C. G. Pappas, I. R. Sasselli, R. V. Ulijn, Biocatalytic pathway selection in transient tripeptide nanostructures. *Angew. Chem. Int. Ed. Engl.* **54**, 8119–8123 (2015).
16. C. Biagini, S. D. Fielden, D. A. Leigh, F. Schaufelberger, S. Di Stefano, D. Thomas, Dissipative catalysis with a molecular machine. *Angew. Chem. Int. Ed. Engl.* **58**, 9876–9880 (2019).
17. H. Che, S. Cao, J. C. M. van Hest, Feedback-induced temporal control of "breathing" polymersomes to create self-adaptive nanoreactors. *J. Am. Chem. Soc.* **140**, 5356–5359 (2018).
18. X. Hao, K. Yang, H. Wang, F. Peng, H. Yang, Biocatalytic feedback-controlled non-newtonian fluids. *Angew. Chem. Int. Ed. Engl.* **59**, 4314–4319 (2020).
19. H. Che, B. C. Buddingh, J. C. M. van Hest, Self-regulated and temporal control of a "breathing" microgel mediated by enzymatic reaction. *Angew. Chem. Int. Ed. Engl.* **56**, 12581–12585 (2017).
20. L. Heinen, T. Heuser, A. Steinschulte, A. Walther, Antagonistic enzymes in a biocatalytic pH feedback system program autonomous DNA hydrogel life cycles. *Nano Lett.* **17**, 4989–4995 (2017).
21. E. Te Brinke, J. Groen, A. Herrmann, H. A. Heus, G. Rivas, E. Spruijt, W. T. Huck, Dissipative adaptation in driven self-assembly leading to self-dividing fibrils. *Nat. Nanotechnol.* **13**, 849–855 (2018).
22. G. Cheng, J. Perez-Mercader, Dissipative self-assembly of dynamic multicompartmentalized microsystems with light-responsive behaviors. *Chem* **6**, 1160–1171 (2020).
23. F. Wang, C. H. Lu, I. Willner, From cascaded catalytic nucleic acids to enzyme-DNA nanostructures: Controlling reactivity, sensing, logic operations, and assembly of complex structures. *Chem. Rev.* **114**, 2881–2941 (2014).
24. F. C. Simmel, B. Yurke, H. R. Singh, Principles and applications of nucleic acid strand displacement reactions. *Chem. Rev.* **119**, 6326–6369 (2019).
25. S. Osborne, Aptamers as therapeutic and diagnostic reagents: Problems and prospects. *Curr. Opin. Chem. Biol.* **1**, 5–9 (1997).
26. G. F. Joyce, Forty years of in vitro evolution. *Angew. Chem. Int. Ed. Engl.* **46**, 6420–6436 (2007).
27. F. Wang, X. Liu, I. Willner, DNA switches: From principles to applications. *Angew. Chem. Int. Ed. Engl.* **54**, 1098–1129 (2015).
28. C. Teller, I. Willner, Functional nucleic acid nanostructures and DNA machines. *Curr. Opin. Biotechnol.* **21**, 376–391 (2010).
29. B. Yurke, A. J. Turberfield, A. P. Mills Jr., F. C. Simmel, J. L. Neumann, A DNA-fuelled molecular machine made of DNA. *Nature* **406**, 605–608 (2000).
30. J. Wang, L. Yue, Z. Li, J. Zhang, H. Tian, I. Willner, Active generation of nanoholes in DNA origami scaffolds for programmed catalysis in nanocavities. *Nat. Commun.* **10**, 4963 (2019).
31. M. Vazquez-Gonzalez, I. Willner, Aptamer-functionalized micro- and nanocarriers for controlled release. *ACS Appl. Mater. Interfaces* **13**, 9520–9541 (2021).
32. M. Vázquez-González, C. Wang, I. Willner, Biocatalytic cascades operating on macromolecular scaffolds and in confined environments. *Nat. Catal.* **3**, 256–273 (2020).
33. T. A. Ngo, E. Nakata, M. Saimura, T. Morii, Spatially organized enzymes drive cofactor-coupled cascade reactions. *J. Am. Chem. Soc.* **138**, 3012–3021 (2016).
34. L. Xin, C. Zhou, Z. Yang, D. Liu, Regulation of an enzyme cascade reaction by a DNA machine. *Small* **9**, 3088–3091 (2013).
35. D. M. Vriezema, P. M. L. Garcia, N. S. Oltra, N. S. Hatzakis, S. M. Kuiper, R. J. M. Nolte, A. E. Rowan, J. C. M. van Hest, Positional assembly of enzymes in polymersome nanoreactors for cascade reactions. *Angew. Chem. Int. Ed.* **119**, 7522–7526 (2007).
36. Z. Zhou, M. Vazquez-Gonzalez, I. Willner, Stimuli-responsive metal-organic framework nanoparticles for controlled drug delivery and medical applications. *Chem. Soc. Rev.* **50**, 4541–4563 (2021).
37. L. Yue, S. Wang, Z. Zhou, I. Willner, Nucleic acid based constitutional dynamic networks: From basic principles to applications. *J. Am. Chem. Soc.* **142**, 21577–21594 (2020).
38. S. Wang, L. Yue, Z. Y. Li, J. Zhang, H. Tian, I. Willner, Light-induced reversible reconfiguration of DNA-based constitutional dynamic networks: Application to switchable catalysis. *Angew. Chem. Int. Ed. Engl.* **57**, 8105–8109 (2018).
39. S. Wang, L. Yue, Z. Shpilt, A. Cecconello, J. S. Kahn, J. M. Lehn, I. Willner, Controlling the catalytic functions of DNAzymes within constitutional dynamic networks of DNA nanostructures. *J. Am. Chem. Soc.* **139**, 9662–9671 (2017).
40. Z. Zhou, L. Yue, S. Wang, J. M. Lehn, I. Willner, DNA-based multiconstituent dynamic networks: Hierarchical adaptive control over the composition and cooperative catalytic functions of the systems. *J. Am. Chem. Soc.* **140**, 12077–12089 (2018).

41. L. Yue, S. Wang, V. Wulf, S. Lilienthal, F. Remacle, R. D. Levine, I. Willner, Consecutive feedback-driven constitutional dynamic networks. *Proc. Natl. Acad. Sci. U.S.A.* **116**, 2843–2848 (2019).
42. L. Yue, S. Wang, S. Lilienthal, V. Wulf, F. Remacle, R. D. Levine, I. Willner, Intercommunication of DNA-based constitutional dynamic networks. *J. Am. Chem. Soc.* **140**, 8721–8731 (2018).
43. J. Deng, A. Walther, Pathway complexity in fuel-driven DNA nanostructures with autonomous reconfiguration of multiple dynamic steady states. *J. Am. Chem. Soc.* **142**, 685–689 (2020).
44. L. Heinen, A. Walther, Programmable dynamic steady states in ATP-driven nonequilibrium DNA systems. *Sci. Adv.* **5**, eaaw0590 (2019).
45. J. Deng, W. Liu, M. Sun, A. Walther, Dissipative organization of DNA oligomers for transient catalytic function. *Angew. Chem. Int. Ed. Engl.* , e202113477 (2022).
46. J. Deng, A. Walther, Fuel-driven transient DNA strand displacement circuitry with self-resetting function. *J. Am. Chem. Soc.* **142**, 21102–21109 (2020).
47. E. Del Grosso, A. Amodio, G. Ragazzon, L. J. Prins, F. Ricci, Dissipative synthetic DNA-based receptors for the transient loading and release of molecular cargo. *Angew. Chem. Int. Ed. Engl.* **57**, 10489–10493 (2018).
48. J. Kim, K. S. White, E. Winfree, Construction of an in vitro bistable circuit from synthetic transcriptional switches. *Mol. Syst. Biol.* **2**, 68 (2006).
49. S. W. Schaffter, R. Schulman, Building in vitro transcriptional regulatory networks by successively integrating multiple functional circuit modules. *Nat. Chem.* **11**, 829–838 (2019).
50. E. Franco, E. Friedrichs, J. Kim, R. Jungmann, R. Murray, E. Winfree, F. C. Simmel, Timing molecular motion and production with a synthetic transcriptional clock. *Proc. Natl. Acad. Sci. U.S.A.* **108**, E784–E793 (2011).
51. J. Kim, E. Winfree, Synthetic in vitro transcriptional oscillators. *Mol. Syst. Biol.* **7**, 465 (2011).
52. E. Del Grosso, L. J. Prins, F. Ricci, Transient DNA-based nanostructures controlled by redox inputs. *Angew. Chem. Int. Ed. Engl.* **59**, 13238–13245 (2020).
53. J. Wang, Z. Li, Z. Zhou, Y. Ouyang, J. Zhang, X. Ma, H. Tian, I. Willner, DNAzyme- and light-induced dissipative and gated DNA networks. *Chem. Sci.* **12**, 11204–11212 (2021).
54. Z. Zhou, Y. Ouyang, J. Wang, I. Willner, Dissipative gated and cascaded DNA networks. *J. Am. Chem. Soc.* **143**, 5071–5079 (2021).
55. S. Wang, L. Yue, V. Wulf, S. Lilienthal, I. Willner, Dissipative constitutional dynamic networks for tunable transient responses and catalytic functions. *J. Am. Chem. Soc.* **142**, 17480–17488 (2020).
56. Y. Ouyang, P. Zhang, H. Manis-Levy, Y. Paltiel, I. Willner, Transient dissipative optical properties of aggregated Au nanoparticles, CdSe/ZnS quantum dots, and supramolecular nucleic acid-stabilized Ag nanoclusters. *J. Am. Chem. Soc.* **143**, 17622–17632 (2021).
57. J. Deng, D. Bezold, H. J. Jessen, A. Walther, Multiple light control mechanisms in ATP-fueled non-equilibrium DNA systems. *Angew. Chem. Int. Ed. Engl.* **59**, 12084–12092 (2020).
58. O. I. Wilner, Y. Weizmann, R. Gill, O. Lioubashevski, R. Freeman, I. Willner, Enzyme cascades activated on topologically programmed DNA scaffolds. *Nat. Nanotechnol.* **4**, 249–254 (2009).
59. O. I. Wilner, S. Shimron, Y. Weizmann, Z. G. Wang, I. Willner, Self-assembly of enzymes on DNA scaffolds: En route to biocatalytic cascades and the synthesis of metallic nanowires. *Nano Lett.* **9**, 2040–2043 (2009).
60. J. Fu, M. Liu, Y. Liu, N. W. Woodbury, H. Yan, Interenzyme substrate diffusion for an enzyme cascade organized on spatially addressable DNA nanostructures. *J. Am. Chem. Soc.* **134**, 5516–5519 (2012).
61. M. Liu, J. Fu, C. Hejesen, Y. Yang, N. W. Woodbury, K. Gothelf, Y. Liu, H. Yan, A DNA tweezer-actuated enzyme nanoreactor. *Nat. Commun.* **4**, 2127 (2013).
62. C. Wang, L. Yue, I. Willner, Controlling biocatalytic cascades with enzyme–DNA dynamic networks. *Nat. Catal.* **3**, 941–950 (2020).
63. S. M. Assadi, M. Yucel, C. Pantelis, Dopamine modulates neural networks involved in effort-based decision-making. *Neurosci. Biobehav. Rev.* **33**, 383–393 (2009).

Acknowledgments

Funding: This research was supported by the Israel Science Foundation (grant no. 2049/20).

Author contributions: Y.O. and I.W. formulated the concepts and methodology of the study. Y.O. and P.Z participated in the experimental work. Y.O., P.Z., and I.W. wrote the paper. I.W. supervised the study. **Competing interests:** The authors declare that they have no financial or other competing interests. **Data and materials availability:** All data needed to evaluate the conclusions in the paper are present in the paper and/or the Supplementary Materials.

Submitted 22 November 2021
Accepted 23 March 2022
Published 6 May 2022
10.1126/sciadv.abn3534